GREEN BANK OBSERVATORY

GBT Memo 314

The New/Upgraded X-Band Receiver for the GBT:Commissioning Report

Larry Morgan, Walter Klahold, Matt Harrison, Paul Marganian

2024 May 24

Abstract

A new/upgraded X-band receiver has been constructed for the GBT with an optimized frequency range of 8 - 12 GHz, although performance is acceptable over 7.2 - 13.0 GHz. System temperatures and receiver temperatures are similar to the previous receiver. The spectral noise response of this receiver is approximately 3% above theoretical and the continuum performance of the receiver is an order of magnitude improved.

1 Summary

The new/upgraded X-band receiver has completed commissioning observations. This report outlines the scientific capabilities of the new receiver and details changes to systems and processes from the previous X-band instrument.

Engineering items which remain outstanding at the time of writing are listed in Appendix B.

1.1 Performance

- System temperatures and receiver temperatures for the new receiver are similar to the previous receiver, with new averages of 26.6 K and 17 K, respectively, in comparison to the previous receiver, which had respective values of 27 K and 18.9 K (values taken from the GBT Observers' Guide and database receiver values, respectively). N.B., the new receiver has been evaluated over a significantly larger frequency range than the previous receiver.

- The response of the new receiver is seen to be reliable (above -3 dB compared to centre of band) from approximately 7.2 GHz to 13.0 GHz. However, above 10.5 GHz this receiver is significantly impacted by RFI, especially in the right circular polarization. Further, cross-polarization effects are seen to increase significantly below a frequency of $\sim$8 GHz.

- The receiver shows excellent baseline stability of the receiver in position-switched mode. Frequency-switched observations are also very stable, although baseline ripples are increasingly evident at larger 'throws'. These baseline ripples are comparable to other GBT receivers and no impact on observational data quality is expected.

Table 1: Performance metrics of the new receiver compared to the old, polarization-averaged

Metric	Old Value	New Value
System Temperature	27.0	26.6
Receiver Temperature (8.0 - 10.5 GHz)	17.3	15.7
Receiver Temperature (8.0 - 12.0 GHz)	18.6	19.9
Spectral Response[a]	$\gtrsim$6%[b]	$\sim$3%
Continuum Response:		
dG/G	6.9 x 10^{-4}	2.8 x 10^{-4}
Noise Ratio	$\sim$3	1.49
$\Delta\nu_{eff}$ (MHz)	21	278

[a]Measured as the ratio of the observed channel-to-channel RMS noise to the ideal radiometer calculated value.
[b]Determined from a small sample of archival observations.

- Polarization observations show minimal to no leakage between polarization channels at a level of -13 dB, with cross-polarization effects estimated to be no greater than -20 dB for a frequency range of 8 to 12 GHz. The polarization switching mode has been tested and seen to work at the hardware level.
- The continuum response of this receiver represents an order of magnitude improvement over the previous one.
- Pulsar mode observations have been tested and found to be operational, with the caveat that there is currently a poorly understood 'lag' in the switching of the high cal noise diode, which is under investigation at the time of writing. This is not expected to impact observational data quality.
- The increased frequency range of the receiver has allowed the Breakthrough Listen project to increase the number of observed frequency bandpasses from three to four. Multiple successful observations using the Breakthrough Listen backend have been performed.
- VLBI observations have been successfully tested
- Tests of the instrument as a radar receiver have been successful and successful observations of objects in lunar orbit have been carried out.

2 Requirements and Comparison to Previous Receiver

In terms of performance, details of individual metrics are outlined throughout the rest of this document. These are summarized here for ease of comparison.

Software Changes

The new/upgraded X-band receiver uses an Odroid/Numato data bus system in order to communicate between the software manager and the hardware. With the exception of some functional testing, this is assumed to be out of the scope of this particular document. The MR describing the implementation of the manager for the new receiver's hardware and the Odroid itself can be found at `https://safe.nrao.edu/wiki/bin/view/GB/Software/ModificationRequest2Q121`

2.1 Narrowband and Wideband Configurations

A notable difference in the hardware configuration of the new receiver is that the nominal IF center frequency is no longer fixed but can be either 4 or 6 GHz depending on the required bandwidth. The reason for this is that most GBT receivers, including the previous X-band receiver, use either a 3 or 6 GHz IF center frequency, which is consistent with filters within the IF rack. However, for a receiver covering the full 8 - 12 GHz range (as opposed to the previous X-band receiver, which, at least nominally covered only 8 - 10 GHz), using these IF center frequencies would potentially lead to issues of poor image rejection and/or RF breakthrough. A full discussion of these issues in relation to the new receiver is described in Klahold (2024), the outcome of which was that the new X-band receiver uses a 4 GHz IF center frequency for 'wideband' observations - wherein the total observed bandwidth is between 1300 and 4000 MHz. For 'narrowband' observations, for which the total observed bandwidth is less than 1300 MHz, the receiver uses a 6 GHz IF center frequency. Note that the threshold of 1300 MHz is somewhat arbitrary, the larger this bandwidth, the greater the degree of RF breakthrough may occur (see Klahold (2024)). Ultimately, a value of 1300 MHz was chosen based largely on the commercial availability of filters. A hardware replacement of this filter could relatively easily be accomplished if so desired in the future, with the caveat that software changes would be necessary to implement the replacement. A further note on the IF selection for the new X-band receiver is that, by selecting an IF center frequency of 4 GHz (i.e. the 'wideband' mode), the IF rack is placed into an 'all-pass' configuration, with possible ramifications for RFI rejection/power stability.

2.2 Software

Most software changes and/or development relating to the commissioning of this receiver are contained within the new manager (see above), changes to the config tool and the development of a user interface for the receiver hardware. This user interface was developed as a 'pyCLEO' window, the MR for which may be found at `https://safe.nrao.edu/wiki/bin/view/GB/Software/ModificationRequest3Q121`.

2.3 Scheduling

It is anticipated that no changes will be required in the scheduling system. 'Good' weather conditions, in the definition used by the Dynamic Scheduling System, cover frequencies 8 - 18 GHz (as well as 27.5 - 50 GHz). Further, while representative opacities may increase by

$\sim$20% over the new range achievable by this receiver, these opacities are still very low ($\tau <$ 0.02) and therefore have minimal impact on observations.

3 Commissioning Tests/Exercises

Commissioning tests of the new X-band receiver were performed in three phases.

- Tests were run in a simulated environment, in order to test software changes and implementation
- 'Live' system tests exploited the prolonged shutdown of the GBT during winter (Jan - March) 2023 for maintenance period tests, which did not necessarily include on-sky, astronomical measurements
- Full commissioning exercises were performed with full control of the GBT and on-sky, astronomical measurements.

Some basic systematic tests were performed throughout all phases of the commissioning. In summary,

- Expected behaviour was seen with regard to the calibration diodes, that is, 'blinking' was as expected for both tp and sp modes, tp_nocal also showed the expected behaviour.
- The IF/LO system correctly configures the 4 or 6 GHz IF center frequency selections for the 'wideband' and 'narrowband' observing configurations, respectively. A flow chart showing the decision tree for this process is shown in Fig.1 and full details are in Modification Request 1Q222[1]
- DCR and VEGAS modes produce appropriate filter bandpasses according to the input configuration.
- It is noted that the narrowband mode operates with an IF centred at 6 GHz, while the wideband mode operates with an IF centred at 4 GHz. Using the DCR and VEGAS backends concurrently in wideband mode should be avoided as this would produce conflicts with the DCR filters, which are centred at either 3 or 6 GHz. This has been recorded in section 4.2.2 of the Proposers Guide (as of April 3rd 2024).

3.1 On-Sky Commissioning

On-sky commissioning tests of the upgraded X-band receiver were carried out between the 16th of November, 2022 and the 10th of February, 2024 by Larry Morgan, Walter Klahold, Matthew Harrison and Paul Marganian. Observations were taken under project codes TGBT22A_501, TGBT22B_610, TGBT23A_613 and TGBT24A_604.

[1] https://safe.nrao.edu/wiki/bin/view/GB/Software/ModificationRequest1Q222

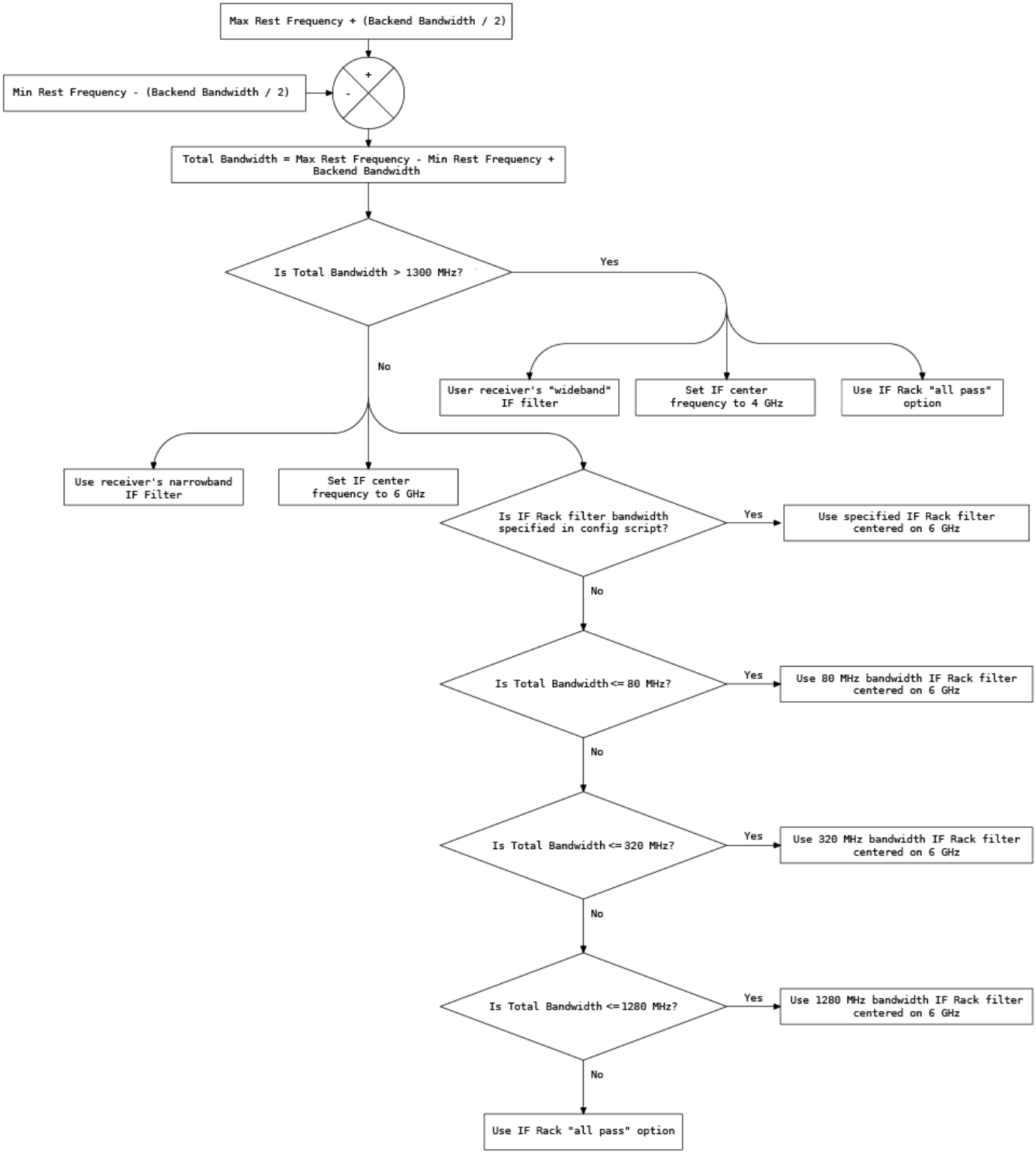

Figure 1: Flow chart describing the IF and associated filter selection algorithm

Table 2: TCal measurements as percentages of the system temperature (database values)

Noise Diode Path	Min.	Max.	Mean	Median
High - LHCP	5.0%	32.9%	22.1%	21.7%
High - RHCP	5.2%	28.1%	18.7%	18.9%
Low - LHCP	1.2%	8.2%	5.1%	5.0%
Low - RHCP	1.2%	6.8%	4.5%	4.7%

3.1.1 TSys, TCal, TRx Evaluation

On-sky reference source observations were performed multiple times throughout commissioning in order to establish the performance of the receiver in terms of its system temperature, receiver temperature and the response of its noise diodes. Observations of 3C196 were taken in the first commissioning sessions to establish approximate values of the 'high' and 'low' levels of the noise diode power levels and these were used throughout commissioning. Later, a more complete and careful set of measurements was taken in order to establish these values more precisely. On the 1st of August, 2023, observations were made of 3C138 and 3C147 across the full band of the X-band receiver (TGBT23A_613_12). These observations were then used to derive the 'TCals' - the temperature equivalent power levels of the noise diodes. The results of these observations showed that,

- Noise diode power levels were stable and the observed frequency-dependent structure was consistent across a period of several hours. A comparison to measurements taken on the 10th of February, 2024 showed that frequency structure was at least superficially consistent over a timescale of months to years.
- Flux levels of observations made in 'Full Stokes' mode were consistent with those made in 'Total Intensity' mode, indicating that there is little to no power leakage between polarization modes.
- Noise diode power measurements were consistent between different reference sources with a sky separation of $\sim$33.5°.

The set of observations established as the current (as of April 2024) reference for noise diode values were performed on 3C138. These were scans 50 - 57 from the project/session TGBT23A_613_12. RFI can be seen in the Right Hand Circularly Polarized (RHCP) data above $\sim$11.5 GHz (also visible in the system and receiver temperature measurements, see Fig.2). Our commissioning observations indicate that this particular grouping of RFI is intermittent but essentially unavoidable (see later note on RFI §3.1.3.5). Table 2 presents the measured values of the various TCal parameters, as percentages of the measured Tsys. While there is some variation over the band, particularly at the low and high edges, TCal values are largely stable at $\sim$5% and $\sim$20% of the system temperature and are consistent between the LHC and RHC polarizations, given the general variation over the band.

Measurements of the system temperature and receiver temperature were determined from the same set of observations used to determine the noise diode values. Plots of these mea-

Table 3: Summary of system temperature and receiver temperature measurements

	Min. (K)	Max. (K)	Mean (K)	Median (K)
TSys - LHCP	21.1	45.7	26.9	24.8
TSys - RHCP	24.5	59.6	32.6	28.4
TRx - LHCP	11.3	35.64	17.0	15.1
TRx - RHCP	14.7	49.5	22.8	18.9

surements, as a function of frequency across the receiver band, are shown in Fig.2 and a summary of the measured values is presented in Table 3.

It can be seen that the RHCP channel is higher in temperature through both system temperature and receiver temperature at levels of approximately 15% and 25%, respectively. This is not necessarily unexpected and similar offsets between receiver temperatures in different polarisation channels can be seen in e.g. the C-band receiver. However, it is noteworthy that offsets between the RHCP and LHCP channels which are seen from on-sky measurements, do not appear when performing the same measurements in the laboratory. Figure 3 shows laboratory measurement values of the receiver temperature for both the LHCP and RHCP channels taken on two separate dates, the 28th of October, 2022 and the 9th of December, 2022. Some difference between values measured on the two dates is attributed to hardware changes in the instrument in the intervening period (new cryostat wiring, replacement of IF amplifiers, etc).

Comparison to Previous Receiver

Receiver temperatures for the new X-band receiver (Fig. 2) are shown in comparison to the previous receiver in Fig. 4. Some general features of the bandpass measurements include known receiver resonances at $\sim$10.5 and $\sim$11.4 GHz for the older receiver, along with notably higher receiver temperatures below a frequency of $\sim$8 GHz. For the new receiver, The RHCP channel shows an offset of $\gtrsim$2 K in comparison to the LHCP channel, with this offset growing to as much as 10 K at some frequencies above $\sim$11 GHz. This increase in RHCP receiver temperature is suspected to be related to instrumentation following the receiver itself in the IF chain (see Fig.3). It is notable that prior receiver resonances have been significantly reduced or eliminated. A comparison of the old and new receiver temperatures is shown in Table 4 for the nominal 'entire' bandwidth of 8.0 to 12.0 GHz as well as the generally used bandwidth of the previous receiver - 8.0 to 10.5 GHz.

3.1.2 Focus/Pointing

Focus observations were performed at a range of frequencies and focus offset positions were in line with expectations throughout commissioning exercises. A search was performed for all focus observations in the X-band frequency range over the period 1st Jan, 2014 to 15th

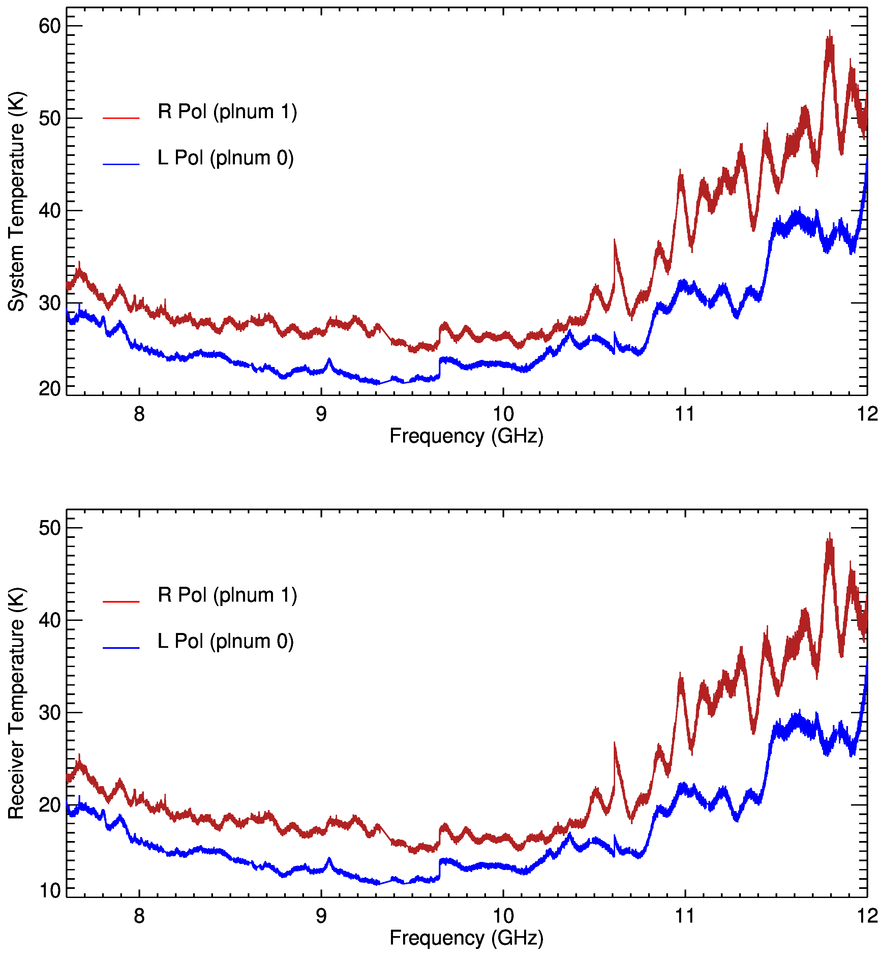

Figure 2: Plots of the system temperature (top) and receiver temperature (bottom) for the RHCP (red) and LHCP (blue) channels of the X-band receiver, as a function of frequency across the receiver band.

Table 4: Comparison of new and old average receiver temperature measurements)

	Receiver Temperature Over Bandpass (K)	
	8.0 - 10.5 GHz	8.0 - 12.0 GHz
Old - LHCP	17.9	19.6
Old - RHCP	16.7	17.7
Old - Average	17.3	18.6
New - LHCP	13.8	17.0
New - RHCP	17.6	22.8
New - Average	15.7	19.9

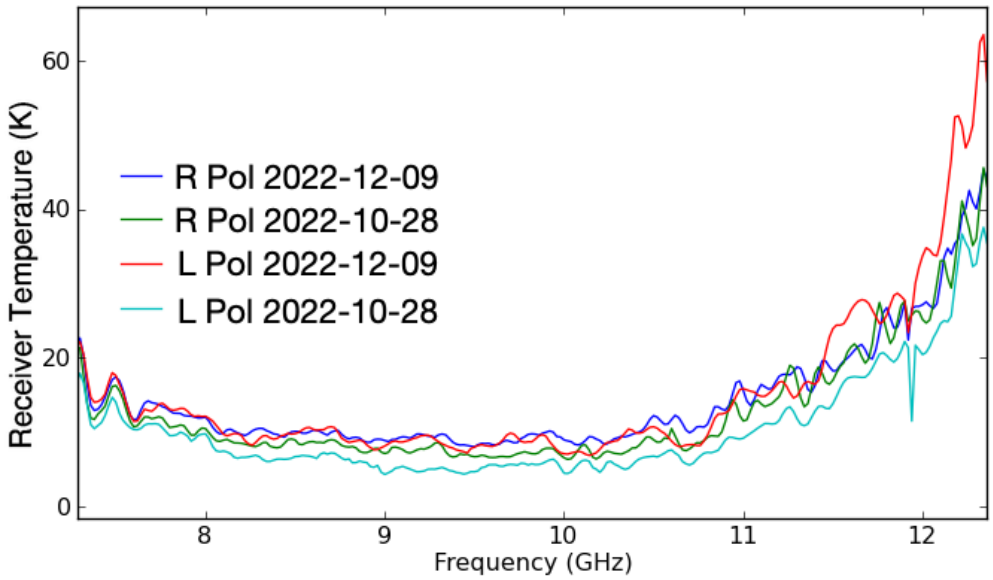

Figure 3: Plot of the receiver temperature for the RHCP (blue/green) and LHCP (red/cyan) channels of the X-band receiver, as a function of frequency across the receiver band. These laboratory measurements were made on the 28th of October, 2022 (green/cyan) and the 9th of December, 2022 (blue/red).

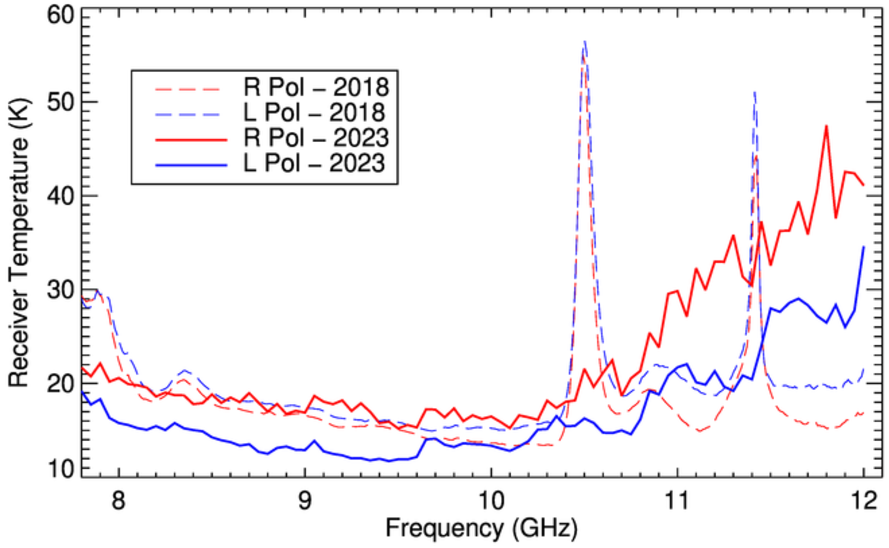

Figure 4: Plot of the receiver temperatures for the new (solid line) and previous (dashed line) X-band receivers, as a function of frequency across the receiver band. These on-sky measurements were made on the 30th of April, 2018 (previous receiver) and the 1st of August, 2023 (new receiver). RHCP measurements are in red and LHCP measurements are in blue

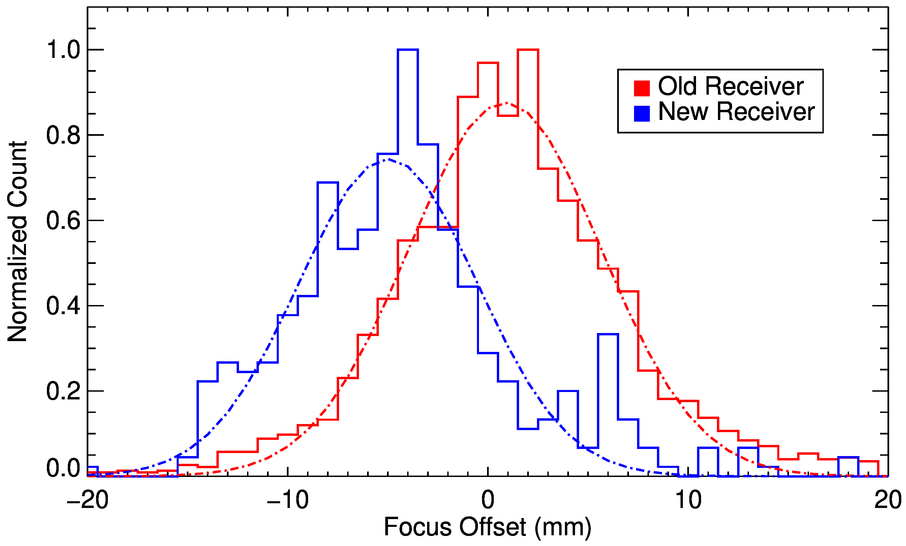

Figure 5: Distribution plot of the local focus corrections measured for a number of scans made with the retired (red) and the new (blue) X-band receivers. The Y-scale represents a normalized count of measurements for each dataset - see main text for details.

April, 2024. A total of 7261 successful[2] scans were found. Scans for which dynamic focus corrections were 0.0 were discarded, as were scans for which the absolute value of the LFC exceeded 20 mm. Figure 5 shows the resulting normalized distributions of 2512 focus scans using the retired X-band receiver and 405 focus scans using the new X-band receiver at 9 GHz. Fits to these distributions indicate that the phase center of the old receiver was at a focus position of approximately 0.85 mm, while the new receiver has a corresponding offset of -4.98 mm. An offset of this degree ($\sim 1.5 \times 10^{-5} \times$ wavelength at 9 GHz) is not necessarily problematic for observations in any way. However, this offset should be accounted for in the 'box-offsets' for this receiver, so that, for example, focus corrections applied as a result of a focus scan at X-band, will also be applicable to receivers at other frequency ranges.

Figure 6 shows the variation of focus offset as a function of observed frequency. The default frequency for X-band focus scans is 9 GHz, resulting in many more scans being represented at that particular frequency. This is evident via the size of the error bars for several of the points in this plot. However, estimations of the variation of focus offset as a function of frequency show values of -3.5 and -3.3 mm/GHz for the old and new X-band receivers, respectively.

It should be noted that, despite the increase in bandwidth of the new X-band receiver in comparison to its predecessor, the default central frequency at which pointing and focus observations will be carried out will remain at 9.0 GHz. All other configuration parameters for default pointing/focus observations (i.e. AutoPeak/AutoFocus/AutoPeakFocus commands) will also remain unchanged. This is to maintain consistency with archival measurements of

[2]'success' here is taken as meaning that the focus corrections were accepted and the corrections were applied to the telescope at the time of the scan.

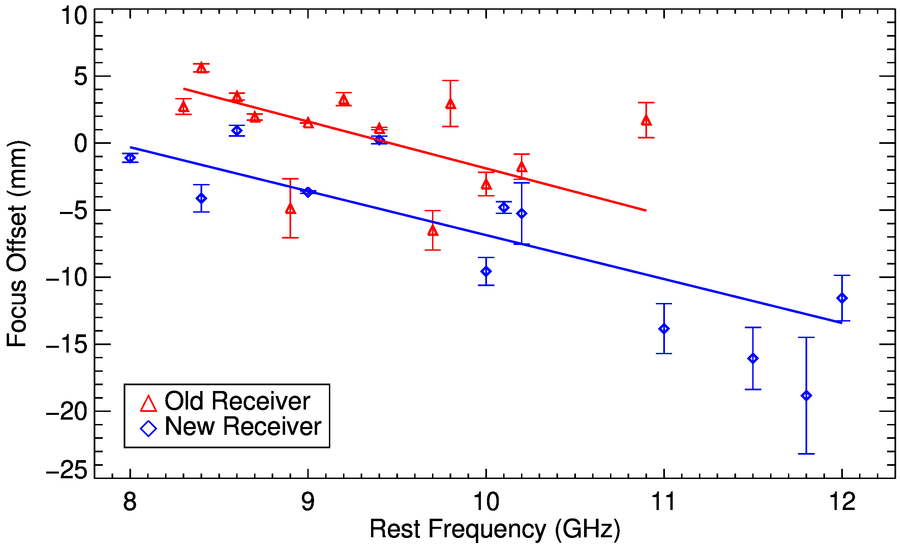

Figure 6: Plot of the variation of local focus corrections as a function of observed frequency measured for the retired (red) and the new (blue) X-band receivers. Error bars represent Poisson estimations ($\sqrt{\frac{Mean}{N}}$)

.

pointing and focus corrections in addition to remaining in a relatively RFI-free portion of the spectrum.

3.1.3 Spectral Line Mode Observations

Commissioning observations in spectral line mode showed correct routing of the IF path, along with consistent selection of the IF center frequency in relation to the narrow-band and wide-band modes. Measurements of the resulting channel-to-channel RMS noise are in line with theoretical predictions.

Spectral Noise Measurements

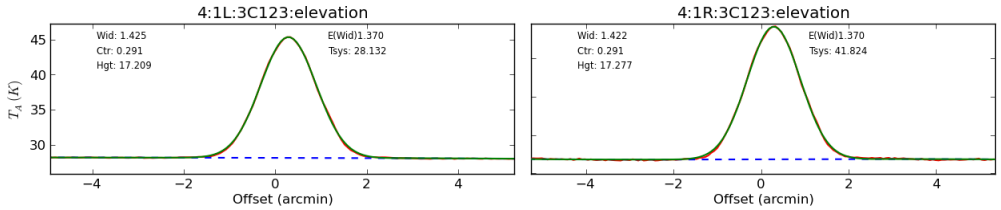

Figure 7: LHCP (left) and RHCP (right) measurements of a peak Scan on 3C123 from the second night of commissioning, the expected flux of 3C123 is 8.73 Jy, yielding approximately 17.5 K at 9 GHz, assuming a gain value for the GBT at 9 GHz of 2.0 K/Jy

Table 5: Comparison between theoretical (ideal radiometer) and measured RMS noise

	RMS over 0.035 s			RMS over 10 m		
	Measured	Ideal	Excess	Measured	Ideal	Excess
LHCP (pl0)	2.71 K	2.64 K	2.85%	20.91 mK	20.20 mK	3.54%
RHCP (pl1)	3.12 K	3.05 K	2.46%	24.05 mK	23.33 mK	3.12%
Averaged	2.05 K	1.99 K	3.02%	15.78 mK	15.27 mK	3.38%

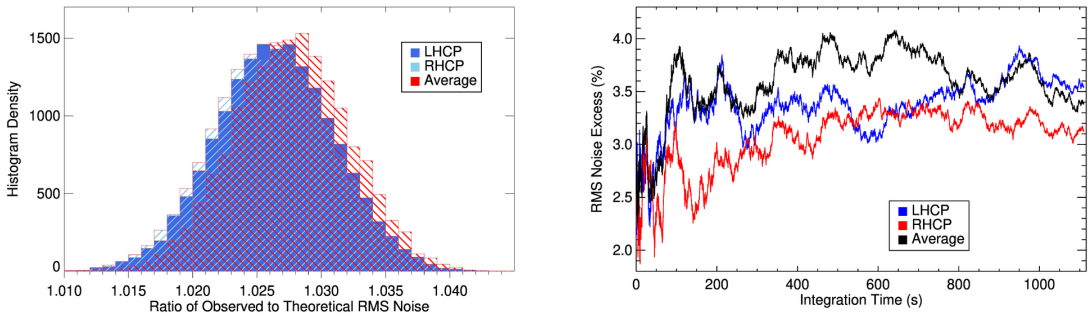

Figure 8: (Left) Histograms of the ratio of observed to theoretical channel-to-channel noise measured for the LHCP (dark blue), RHCP (light blue) and averaged (red) polarization channels. (Right) Ratios of observed to theoretical channel-to-channel noise as a function of accumulated integration time, with LHCP, RHCP and averaged data shown in blue, red and black, respectively.

Blank sky observations were performed to confirm the spectral noise response of the receiver. Fig.8 (left) shows histograms of the ratio of measured to predicted RMS noise over 17166 integrations of scans taken on the 20th of September, 2023 under project/session ID TGBT23A_613_18. For each polarization (and average), these histograms show the distribution of the ratio of measured RMS noise in a given individual integration (of 0.035 s) to the corresponding theoretical (ideal radiometer) noise calculation. Table. 5 gives the absolute values relating to these distributions, along with corresponding values reached after 10 minutes of integration time. These, along with the left plot of Fig.8 show that spectral line observations with this receiver are achieving channel-to-channel RMS fluctuations at a level of approximately 3% above an ideal radiometer. The right plot of Fig.8 shows the variation of the ratio of measured to predicted RMS over total integration time for accumulated scans. This shows that the level of excess of measured to predicted RMS increases slightly over longer periods but remains stable at ∼3% for integration times of at least 10 minutes.

3.1.3.1 Spectral Line Detection

The results of GBT observations of the C_4H spectral line at 9497.616 MHz towards TMC-1 are shown in Fig. 9. Position-switched observations were taken during commissioning exercises on the 14th of June, 2023 and are shown in red in the left plot of Fig. 9. Frequency-switched observations were taken during commissioning exercises on the 10th of February,

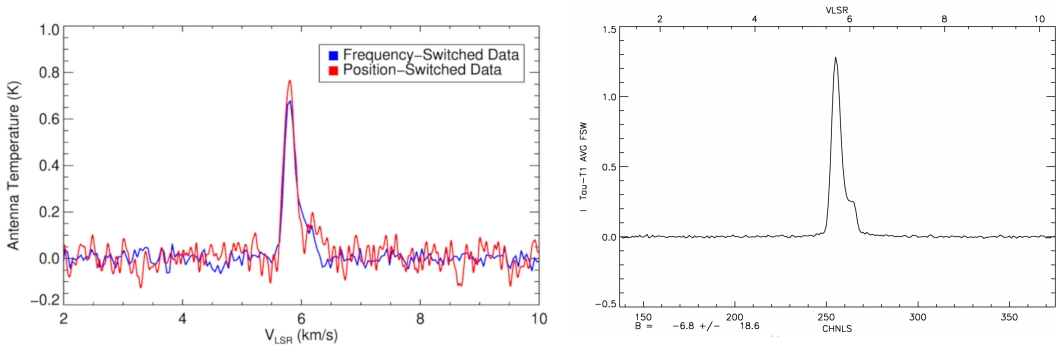

Figure 9: GBT observations of C_4H molecular spectral line emission from the TMC-1 molecular cloud. On the left are shown observations taken during commissioning exercises with position-switched data shown in red and frequency-switched data shown in blue. Right is an observation of the same position at the same frequency, made with the GBT in 2003 and published in Turner & Heiles (2006). Note that the scale in the data of Turner & Heiles (2006) is for *Stokes I*, see main text.

2024 and are overlaid in blue in the same plot.

The right-hand plot shown in Fig. 9 is taken from Turner & Heiles (2006), who used the GBT in 2003 to observe the same sky position at the same frequency. It can be seen that the line profile, observed velocity and line strength[3] are all matched well, given that the integration time of the observations presented in Turner & Heiles (2006) is stated as 34.7 hours, while the total integration times used for our commissioning observations are only ∼6 and ∼16 minutes for the position-switched and frequency-switched observing modes, respectively. The reported velocity resolution of the observations presented in Turner & Heiles (2006) is 0.04 km/s, approximately equal to the 0.036 km/s of the presented frequency-switched data. The position-switched data were smoothed to this same resolution.

3.1.3.2 Bandpass Measurements

Blank-sky observations were performed on the 2nd of February, 2023 under the Project/Session code TGBT22B_610_06 in wideband mode in order to determine the frequency response of the receiver close to the nominal band edges. Fig. 10 shows the total power response at the low- and high-frequency edges of the band. The receiver response at the low end of the band decreases more steeply than at the high end. The receiver response decreases by ∼3 dB at 7.2 and 13.0 GHz for the low and high ends of the receiver band, respectively. Within each of the plots of Fig. 10 is a dotted vertical line which shows the commanded central frequency of the band.

The goal in defining Band 'edges' here is to provide a direct measurement of the response of the receiver itself, not limitations imposed by filters or mixers in the signal path. With that in mind, it should be noted that this drop-off will be due to some combination of the edges of the pre-mixer bandpass filter (8-12 GHz) and the wideband post-mixer bandpass

[3]It should be noted that Turner & Heiles (2006) present the data as *Stokes I*, i.e. the LHCP and RCHP channels have been summed, rather than averaged, as with the data presented here. This will account for a factor of two between the datasets.

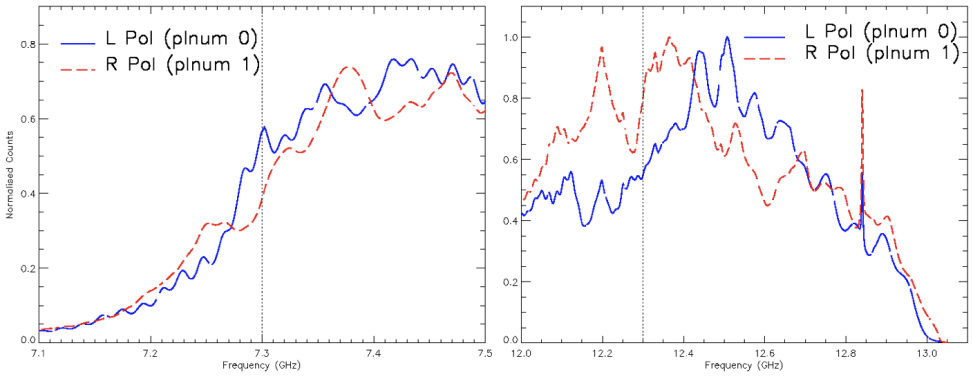

Figure 10: The total power response of the receiver at the low- (left) and high- (right) frequency edges of the receiver band. The y-axis is normalised to the peak emission in the observed frequency window. A vertical dotted line indicates the commanded observed central frequency of the band.

filter (2-6 GHz) - see the block diagram of the receiver in Appendix A.

For the low end of the receiver, observed frequencies of 7.3 and 8.3 GHz were used, centring the IF at 4.5 GHz. It is possible that centring the IF in the exact centre of the bandpass filter at 4.0 GHz would allow this lower end of the receiver response to be driven down further. It is also possible that further or alternative lower tunings might be achieved using the narrowband mode, i.e. with the post-mixer filter centred at 6 GHz. However, as this would require specialized configurations beyond the standard observing requirements (if only in that commanded frequencies would need to be carefully selected and no warning would necessarily be generated if these were not correct), then the presented observations represent a robust nominal lower range of observable frequencies using this receiver.

At the high end of the frequency range, receiver response decreases steeply at ∼13.0 GHz. This is likely due, fully or in part, to the 1.85 GHz bandwidth filtering that occurs in the converter modules and so should not be taken as a completely robust upper limit to the receiver response. The receiver itself may not be absolutely limited to an upper frequency limit of 13.0 GHz. However, measured system temperatures climb rapidly above ∼12 GHz and this would likely limit many applications above this frequency.

3.1.3.3 Baseline Stability

Multiple series of scans were observed throughout commissioning in order to test the stability of the baseline shapes produced by the receiver. These were observed in position-switched and frequency-switched modes with a variety of integration times. Figure 11 shows an example of 'stacked' spectral line observations, taken in frequency-switched mode with a frequency 'throw' of 1 MHz. Inconsistencies between adjacent or close-by scans are typically visually evident, as is demonstrated by the RFI seen at, e.g. the three lines between ∼8.0 and 8.2 GHz.

Visual inspection of frequency- or position- switched scans stacked in this way revealed no systemic discrepancies or drift in baseline shapes over bandwidths of 11.72, 23.44, 187.5 and 1500 MHz. This was true for frequency switch 'throws' of 1, 5, 10, 15 and 20 MHz. The

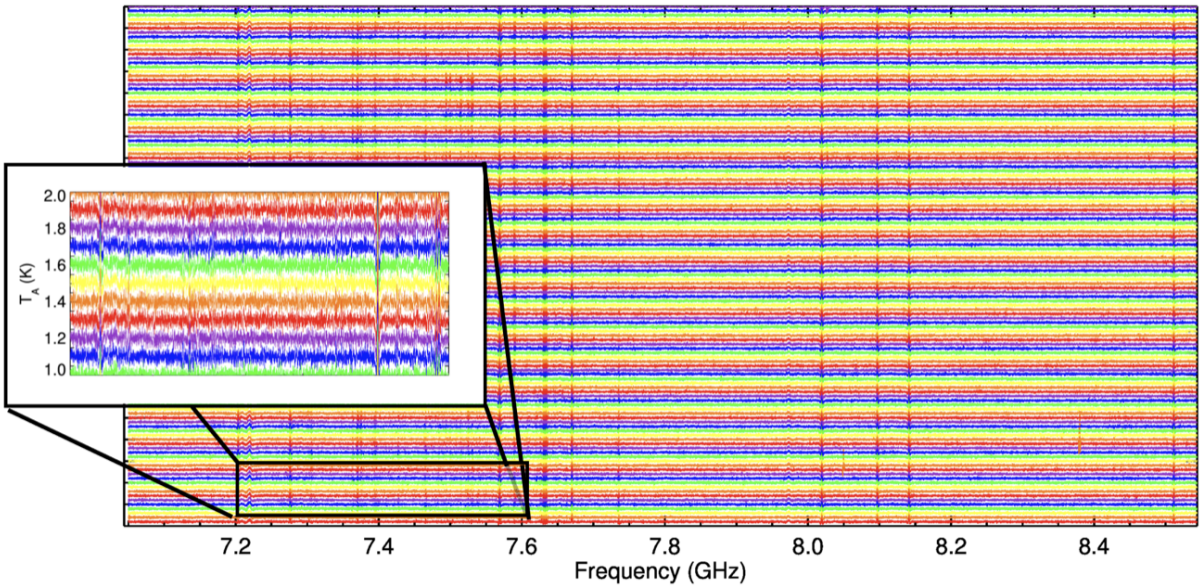

Figure 11: Frequency-switched scans stacked with a separation of 0.2 K, the inset image shows a magnified section of the stack with a separation of 0.1 K. The frequency 'throw' used in these observations was 1 MHz

example shown in Fig. 11 uses observations with a frequency throw of 1 MHz. Inspecting observations made with frequency throws of up to 20 MHz showed that, while the amplitude of baseline ripples increase with frequency throw, (see Fig 12), such ripples are generally consistent in shape (and therefore easily removable via polynomial baseline fitting).

3.1.3.4 Polarization

The new X-band receiver is constructed such that it is natively capable of receiving and distinguishing between left and right circularly polarized radiation. In addition to observations of the individual, separate polarizations this also enables the observation of full Stokes parameters, as well as the specialized observing mode of polarization-switching.

Observations were taken in order to determine the polarization response of the receiver. The spacecraft Voyager 1 emits a signal of 100% left-circular polarization at 8420.2 MHz. On the 10th of February, 2024, Voyager 1 was observed in position-switched mode under project/session code TGBT24A_604_01. The resulting spectral response can be seen in Fig. 13 and the signal from Voyager 1 is apparent in this plot. It is noted that the polarizations of the X-band receiver were originally mis-labelled and that, in May 2023 the receiver was removed from the telescope and the polarisations were corrected via the rotation of the receiver's waveguide phase shifter through 90°.

Full Mueller matrix measurements of the cross-polarization characteristics of the receiver were not performed as part of commissioning exercises. However, by considering individual components of the receiver where cross-polarization can occur, the combined X-band receiver and GBT optics system is expected to produce cross-polarization at a level of -20 dB (1%) at worst, for a frequency range of 8 to 12 GHz. The dominant contribution to this being the

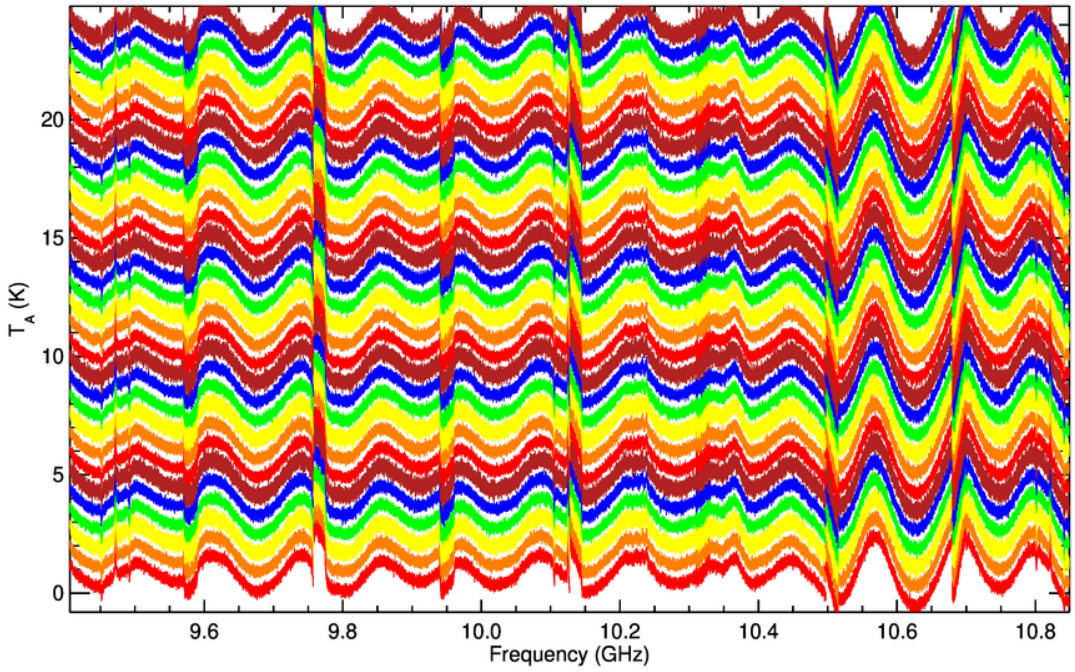

Figure 12: Frequency-switched scans stacked with a separation of 0.8 K. These scans were observed with a frequency-switch of 20 MHz.

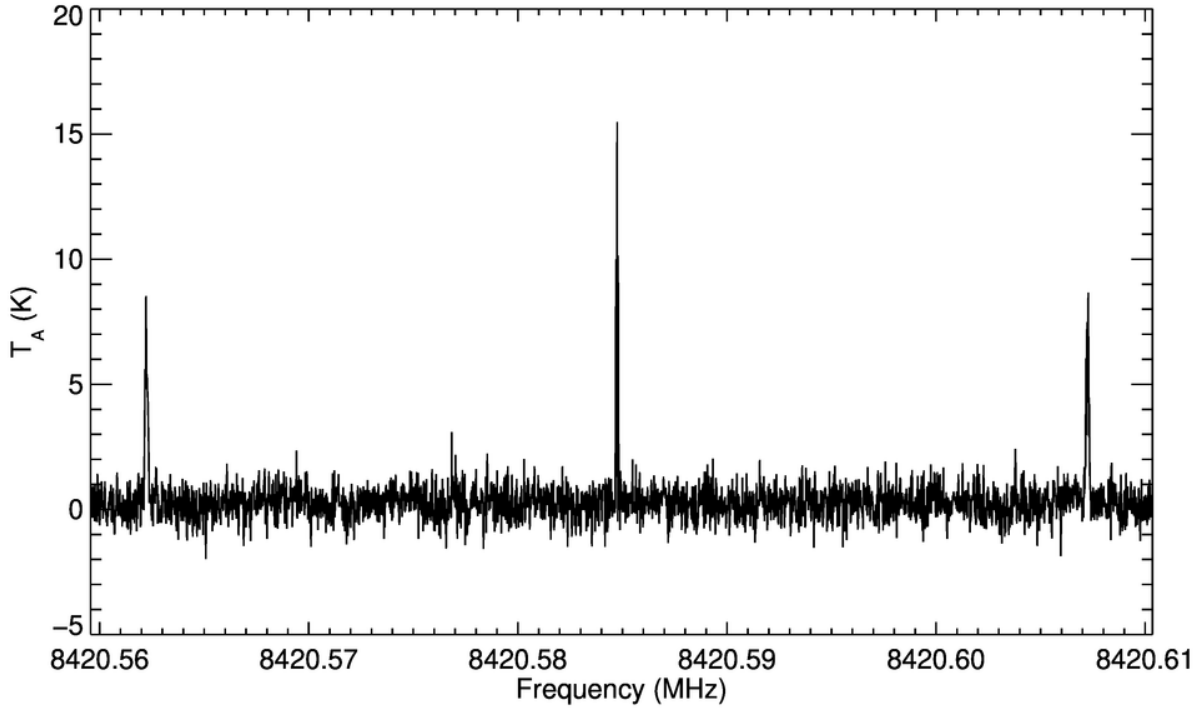

Figure 13: Position-switched observation of Voyager 1, showing the LHCP transmission signal at 8420.2 MHz

deviation of the phase shifter phase shift from 90 degrees. A full description of this estimate is presented in Klahold (2024)

In order to test for 'leakage' between polarization modes, measurements of the noise diodes were performed in full stokes mode. Comparison of these scans with noise diode calibration observations made in regular mode does not show any significant discrepancies. Further, observations of the Voyager 1 carrier signal (Fig.13) resulted in a detection peak of 15.43 K in a single spectral channel in the LHCP data. The RHCP data do not show any evidence of this peak to an RMS limit of 0.66 K, this suggests that any polarization leakage that may be occurring is at a level of -13 dB or below.

Polarization-switching observations were performed and hardware operations were as expected. That is, the transfer switch in the receiver, which functions to cross the signal paths from the nominal RHCP and LHCP feed inputs at a point immediately following the cryogenic dewar, was reported to switch as commanded. Observational tests to confirm the operation of the polarisation-switching were inconclusive. A search for previous observations using this mode was performed in order to establish a benchmark against which to compare our measurements. However, no scans of any kind were found in the entire observational archive. Furthermore, GBT experts were consulted (F.Ghigo, P.Taylor, A.Minter) and no use cases for this mode could be provided.

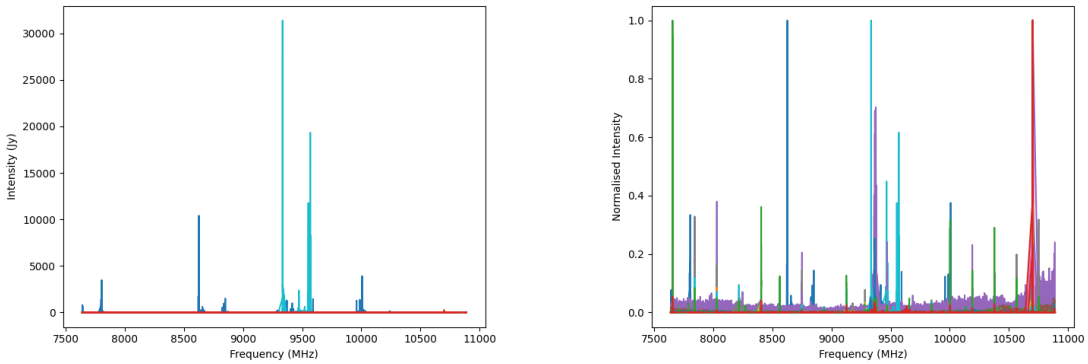

Figure 14: A plot of the RFI environment between 7.6 and 10.9 GHz from scans made using the GBT between the 9th of November 2021 and the 7th of September 2022, the left plot shows the uncorrected intensity of RFI spikes, while the right plot shows the normalised intensity.

3.1.3.5 RFI

Figure 14 shows archival RFI scan data at X-band for the GBO site for the period 9th November 2021 - 7th September 2022. The left-hand plot shows the uncorrected intensity of the RFI spikes and the right-hand plot has a normalised intensity scale. The identification of the sources of each of these signals is beyond the scope of this document. However, we are able to determine if signals seen during commissioning exercises are pre-existing. As an example, Fig. 15 shows a stacked plot of a set of scans observed on the 3rd of February, 2023 - some noteworthy features are the multiple lines seen in essentially all scans between ∼9.3 and 9.5 GHz, as well as a particularly strong, but transient line seen at ∼9.58 GHz. These features are all consistent with previously observed RFI at these frequencies and are within the FCC-allocated band for Earth exploration satellites (active), radiolocation, radionavigation, space research (active) and meteorological aids. Also observed (not pictured) is the 10.7 GHz source known to arise from the GBT's holography receiver.

As the new X-band receiver is expanding upon its predecessor's observable bandwidth, it is expected that previously unobserved sources of RFI will be observed above ∼10.8 GHz. As Fig. 16 shows, we see such emission. Approximately 200 MHz 'chunks' of increased emission are visible, ranging from ∼11.0 to 11.7 GHz. These chunks appear to correspond to *Starlink* satellite transmission channels, which are the subject of concentrated investigation through GBO and National Radio Dynamic Zone staff. A more thorough analysis is presented in the NRAO RFI Memo (DePree et al., 2023).

3.1.4 Continuum Mode Observations

A primary goal of these commissioning exercises was to establish the stability and quality of the receiver's continuum response. The primary metric for determining the continuum response of the new X-band receiver is the 1/f noise floor. Here we follow the methodology of Mason (2013), which uses the fractional gain fluctuation in comparison to the radiometer

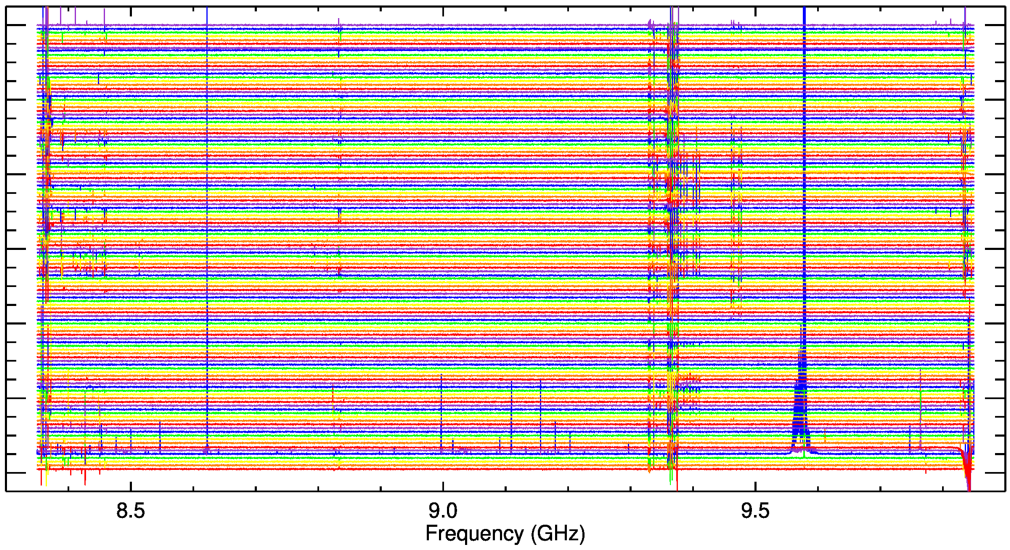

Figure 15: A stacked set of position-switched spectral line observations of 'blank sky' observed on the 3rd of February, 2023

equation prediction of thermal noise, i.e.

$$\left(\frac{\Delta G(f)}{G}\right)^2 = \left(\frac{\Delta T}{T_{sys}}\right)^2 - \frac{1}{\Delta\nu\tau} \tag{1}$$

where $\Delta\nu$ is the bandwidth of the observation in question and τ is the integration time per sample. In addition, we also present the ratio of the observed noise to the expected radiometer (thermal) noise

$$\text{Noise Ratio} = \frac{\Delta T}{T_{sys}}\sqrt{\Delta\nu\tau} \tag{2}$$

and the effective radiometer bandwidth

$$\Delta\nu_{eff} = \left[\left(\frac{\Delta G}{G}\right)^2 \tau\right]^{-1} \tag{3}$$

which is the bandwidth of an observation made by an ideal radiometer in the same integration time which would show the equivalent level of RMS noise.

A determination of these parameters from data taken during commissioning shows a significant improvement of the 1/f noise in all metrics over the previous X-band receiver. On the 30th of April 2023 continuum scans were taken during the session TGBT23A_613_02, yielding the results shown in Table. 6. These data were taken with a bandwidth of 80 MHz and an integration time of 0.1 s. The results of Mason (2013) for the previous X-band receiver are also shown in Table. 6 (the value of noise ratio is estimated as this is not explicitly stated in the memo).

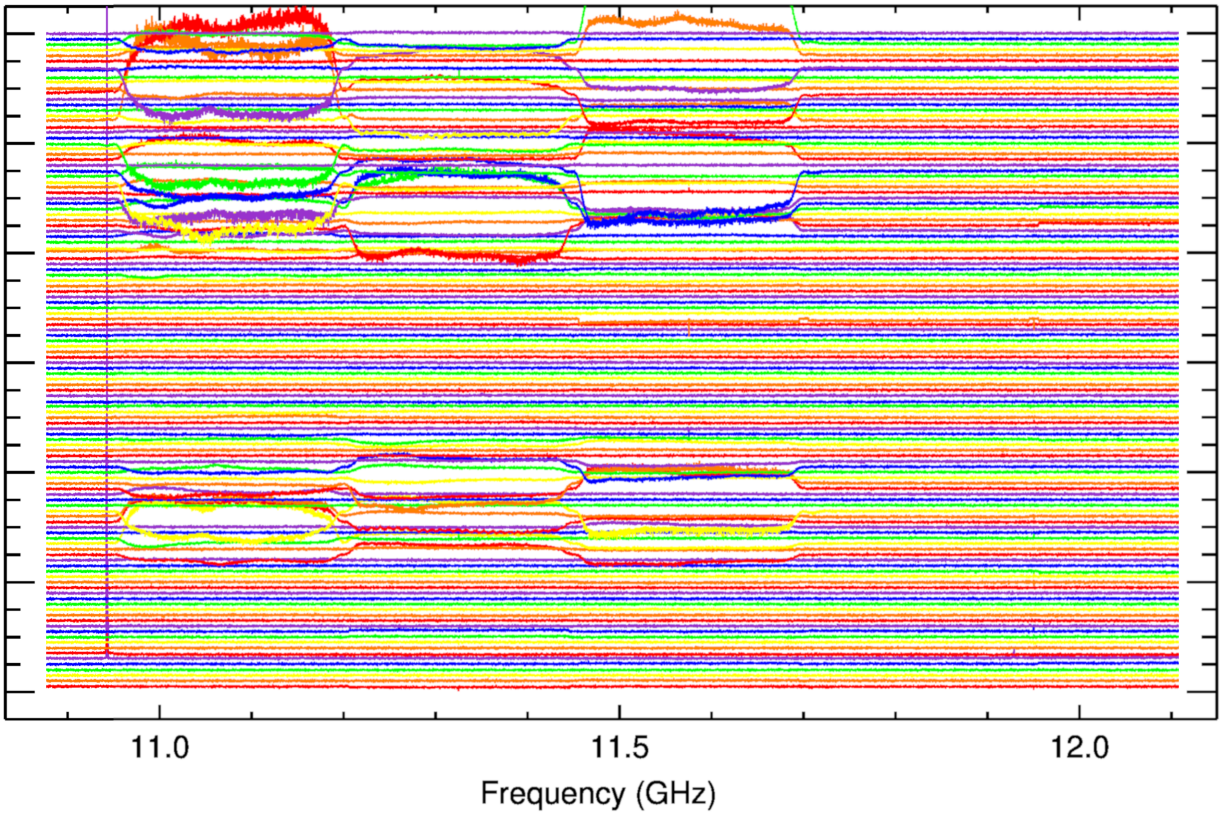

Figure 16: A stacked set of position-switched spectral line observations of 'blank sky' observed on the 3rd of February, 2023. This plot shows suspected RFI emission from the *Starlink* satellites.

Table 6: 1/f noise measurements for observations taken on the 30th of April 2023

	Polarisation 0	Polarisation 1	Previous X-band Receiver Value
dG/G	2.8 x 10^{-4}	2.5 x 10^{-4}	6.9 x 10^{-4}
Noise Ratio	1.14	1.12	$\sim$3
$\Delta\nu_{eff}$ (MHz)	260	327	21

Table 7: 1/f noise measurements from PTCS observations taken on the 5th of May 2023

	Polarisation 0			Polarisation 1		
	mean	median	std.dev	mean	median	std.dev
dG/G	2.7 x 10^{-4}	2.5 x 10^{-4}	1.1 x 10^{-4}	3.2 x 10^{-4}	3.1 x 10^{-4}	1.0 x 10^{-4}
Noise Ratio	1.48	1.39	0.34	1.62	1.58	0.33
$\Delta\nu_{eff}$ (MHz)	377	340	210	264	216	160

Further data taken during a 12-hour PTCS run on the 5th of May, 2023 were analysed. These data were taken with an integration time of 0.1 s and a bandwidth of 320 MHz. Figure 17 shows the resulting distributions of gain fluctuations and noise ratios for the different polarizations of the X-band receiver. These plots show results consistent with the values in Table. 6. The means, medians and standard deviations of these distributions are recorded in Table. 7. The similarity of mean and median values, along with small comparative standard deviations for the parameters of dG/G and noise ratios indicates that these values are robust. A larger relative scatter for values of effective bandwidth, $\Delta\nu_{eff}$ is believed to be due to the pointing scans used for this analysis being taken with a filter bandwidth of 320 MHz, compared to the default of 80 MHz.

These results represent a large improvement in continuum response over the previous receiver, with X-band now being second only to Ku-Band in terms of non-specialised continuum receivers.

3.1.5 Pulsar Mode Observations

Test observations were made using the VEGAS pulsar mode to ensure that the coherent, incoherent and search modes were all operational. An example pulse observation of the source B0355+54 is shown in Fig. 18. These observations were largely without issue with the exception of those using the 'high' cal noise diode. Like nearly all observations made with the GBT, pulsar mode measurements are performed with a noise diode firing at a rate of half the integration time. The response of this noise diode is normally fast enough to be considered instantaneous on the scale of the integration time. Fig. 19 shows the observed flux level during an observation of B0355+54, using the 'low-cal' noise diode. The difference between the 'cal-off' and 'cal-on' phases can clearly be distinguished in the difference between the flux level, shown in white, above and below a pulse phase of 0.5. While some gradient of can be seen between the two phases, this change appears to be very rapid on the scale of the plot. The cal cycle has a rate of 0.04 s here, i.e. 20 ms on, 20 ms off. The difference between the cal-on and cal-off phases here is approximately 0.01 of the pulse phase, so approximately 0.4 ms.

By comparison, Fig. 20 shows the cal response from the 'high' cal noise diode. A much slower 'roll-off' of the cal flux level can be seen, taking approximately 5 ms to reach its full power level. From consultation with R.Lynch, pulsar mode observations using the high-cal noise diode are likely to remain valid, given this issue. However, the reduction of these data would need to be done carefully and would require some non-standard reduction techniques.

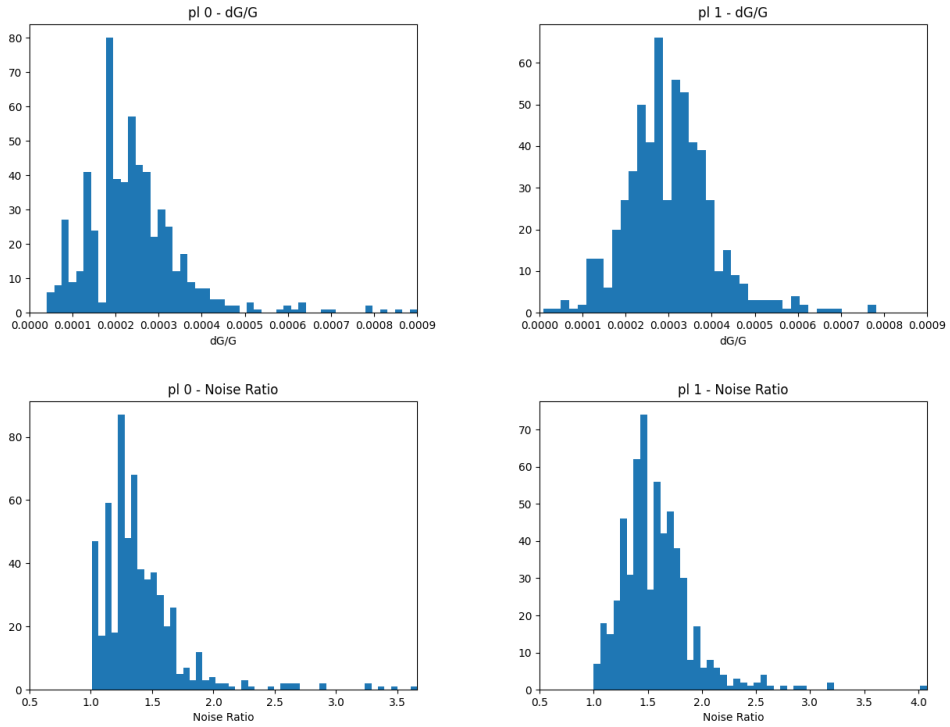

Figure 17: Distributions of values of gain fluctuations (top) and noise ratio (bottom) for polarisation 0 (left) and polarisation 1 (right), determined from TPTCS230505 observations.

Pulsar observers using the new X-band receiver are advised to use the low-cal only until this problem can be remedied.

3.1.6 Other Backends

In addition to the DCR and VEGAS, the GBT operates (or provides support for the operation of) three other backends in regular use in combination with the X-band receiver. These are the Breakthrough Listen backend, the VLBI backend and the JPL radar backend.

3.1.6.1 The Breakthrough Listen Backend

Breakthrough Listen operate a multi-wavelength observing campaign on the GBT using a backend of their own design and manufacture (MacMahon, et al, 2018 [4]). Their observing strategy involves recording of the raw voltages, which are digitized before processing. Multiple observations were taken using the Breakthrough Listen backend in order to test that compatibility was maintained with the new receiver. No issues were encountered which might hinder observations and data analysis shows that results are of a comparable quality to those taken with the previous receiver.

3.1.6.2 VLBI

Test VLBI observations were performed in conjunction with several other VLBA stations in

[4]https://ui.adsabs.harvard.edu/abs/2018PASP..130d4502M

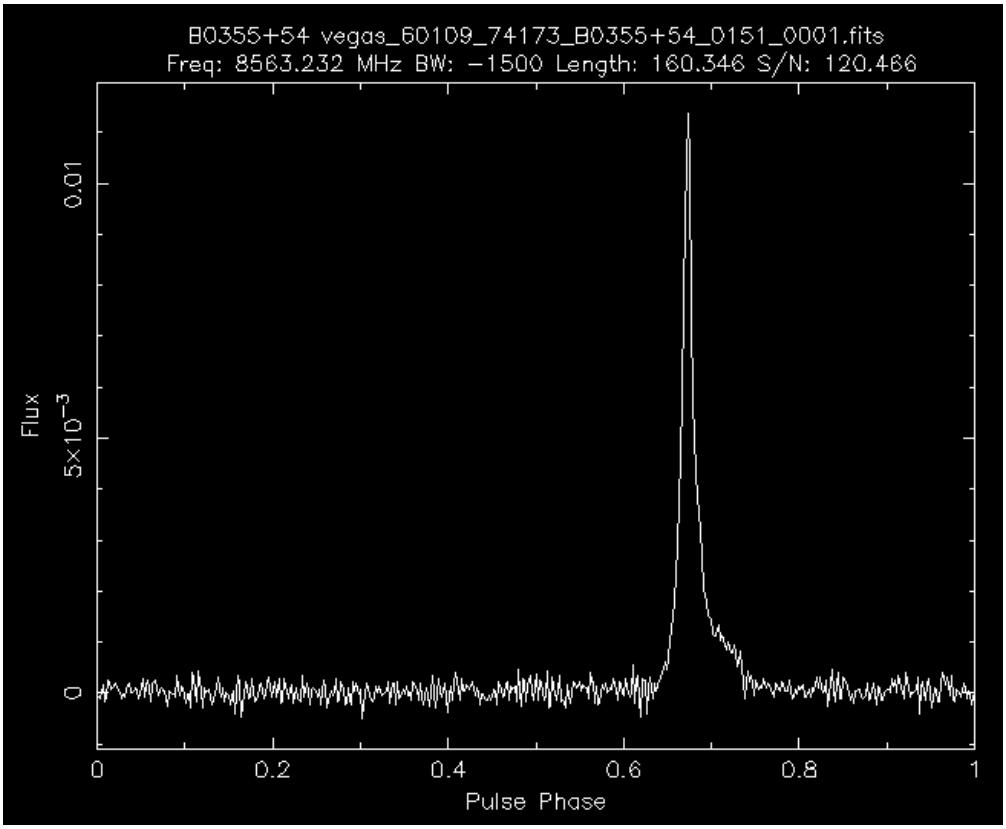

Figure 18: Pulse profile of the pulsar B0355+54, a standard and well-known source

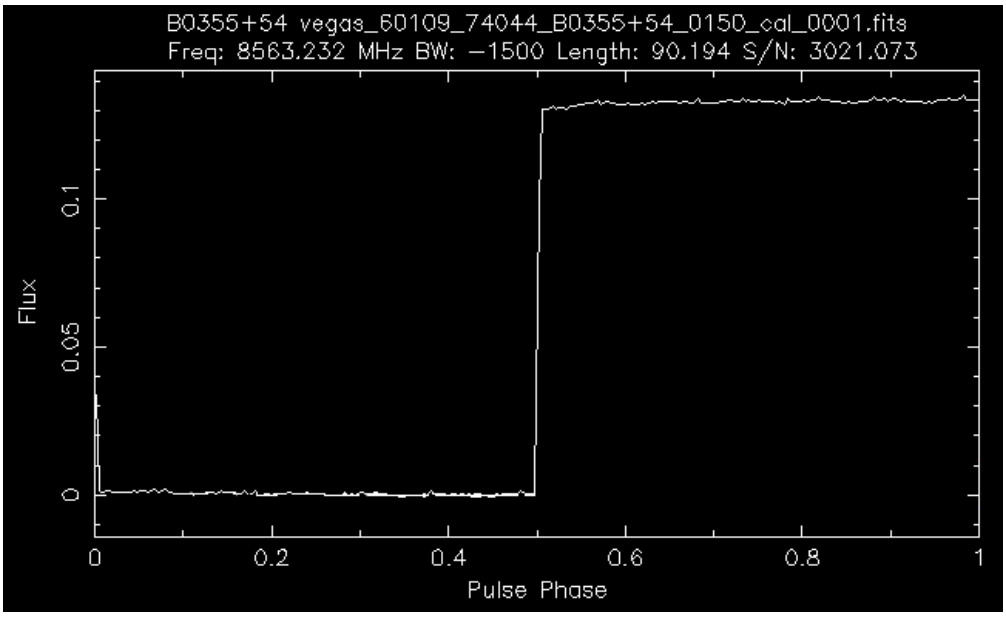

Figure 19: A plot showing the pulse phase of an observation made toward B0355+54. The white line shows the observed flux level associated with the low cal noise diode.

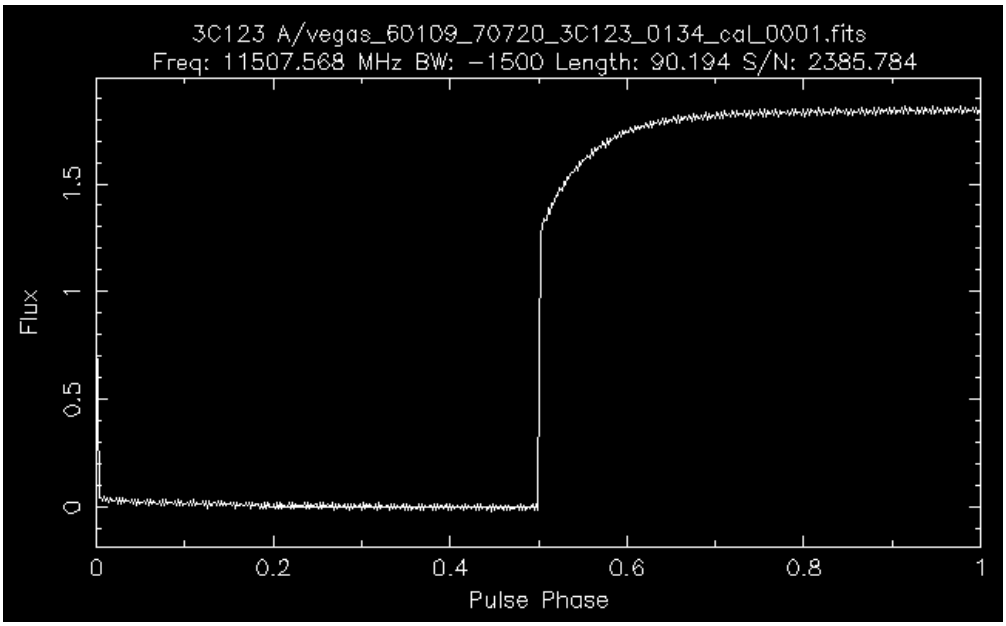

Figure 20: A plot showing the pulse phase of an observation made toward 3C123. The white line shows the observed flux level associated with the high cal noise diode.

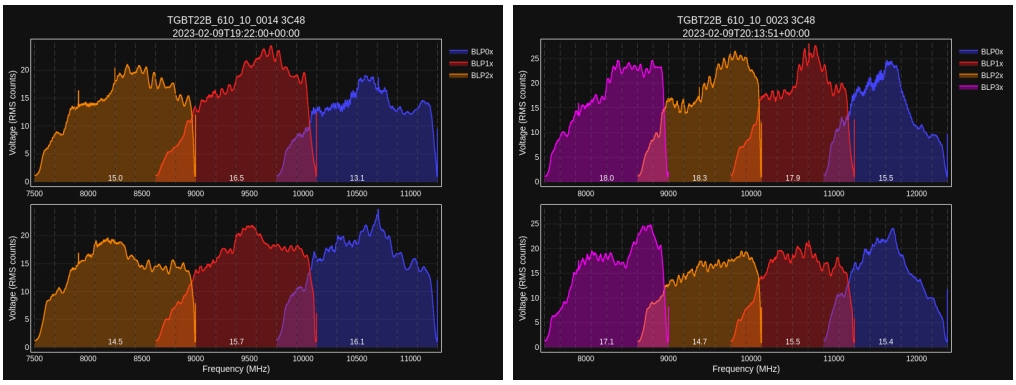

Figure 21: Breakthrough backend plots of observed bandpasses using the old X-band receiver configuration (left) and the new receiver configuration (right) which has an additional bandpass exploiting the increased observable bandwidth.

order to check for the detection of fringes. Observations were taken on the 10th of February, 2024 with the GBT and the VLBA stations in Kitt Peak, Hancock, Fort Davis, Brewster and Los Alamos. Results were positive, with good phase stability and high signal-to-noise for the Green Bank baselines.

3.1.6.3 Radar

Initial tests of the JPL backend were performed on the 16th of February, 2023. A test tone was injected via the LO and a spectrum analyzer was used to investigate the output of the JPL backend and check that the tone was visible to that backend. The tone was observed at the correct input frequency. The input tone was varied in frequency and power and corresponding changes in the output of the JPL backend were observed.

Subsequent to this, a session of radar observations was observed with the new X-band receiver. These observations were taken during poor weather (rain), which likely accounts for the high Tsys seen ($\sim$52 K). However, the lead observer for this project has stated that ''the observed radar track on June 16 was successful. We detected the Lunar Reconnaissance Orbiter and Chandrayaan-2 in lunar orbit. The spurs that were mentioned before the track did not appear in the target echo images."

References

DePree, C., Armentrout, W., Beasley, T., et al. 2023, NRAO RFI Memo Series #154

Klahold, W. 2024, GBT Memo Series #311

Mason, B. 2013, GBT Memo Series #282

Turner, B. E., & Heiles, C. 2006, ApJS, 162, 388, doi: 10.1086/498431

Appendix A:

X-Band Receiver Block Diagram

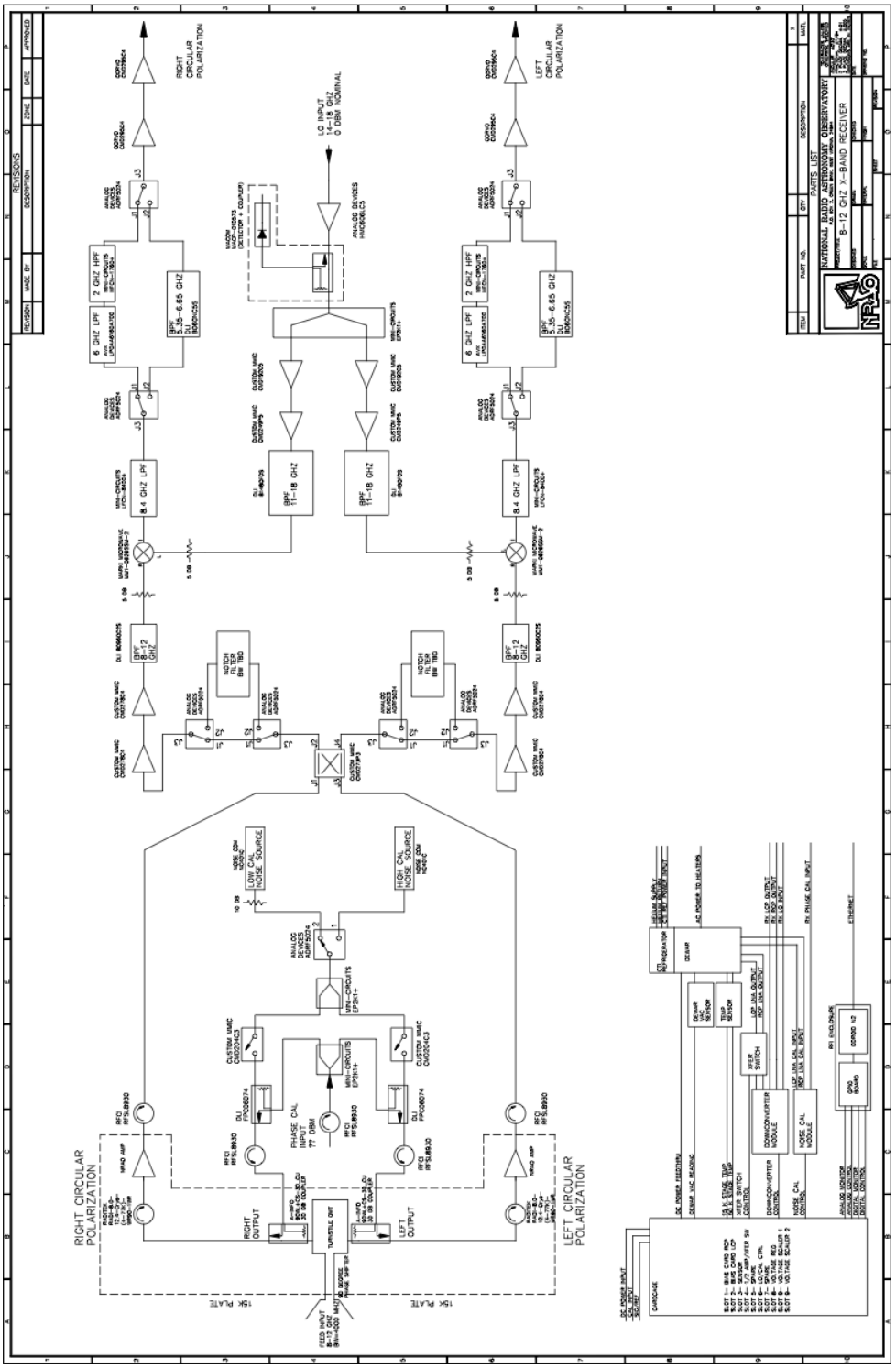

Appendix B:

Issues Under Continuuing Investigation

- We are seeing spikes in the data which are almost certainly due to instrumentation. These have not impacted data quality of any projects run so far as they are very stable and so are subtracted out in position-switched data. These will be investigated during summer shutdown, 2024.
- Differences between receiver temperatures in the L and R polarization channels persist. Indications are that these are instrumental and may also impact C-band. This issue does not currently severely impact data quality but efforts will be made to at least isolate the cause.
- The 9 GHz focus offset (-4.98mm) should be accounted for in the box offsets of the receiver, this will be passed to SDD.
- Polarization-switching tests were at least partially inconclusive. Further observations of Voyager 1 and possible comparisons using L-band following summer shutdown 2024 should resolve this.
- The 'roll-off' of the high-cal noise diode needs to be investigated. This is reliably reproduced with both scientific and engineering observations with the receiver installed on the telescope. Further tests will be made during summer shutdown, 2024.